

Dilution of a polar magnet: Structure and magnetism of Zn-substituted $\text{Co}_2\text{Mo}_3\text{O}_8$ L. Prodan ^{1,2}, I. Filippova ², A. O. Zubtsovskii ³, S. Shova,⁴ S. Widmann,¹
A. A. Tsirlin ^{3,5}, I. Kézsmárki,¹ and V. Tsurkan ^{1,2}¹*Experimental Physics V, Center for Electronic Correlations and Magnetism, Institute of Physics,
University of Augsburg, D-86159 Augsburg, Germany*²*Institute of Applied Physics, MD 2028 Chişinău, Republic of Moldova*³*Experimental Physics VI, Center for Electronic Correlations and Magnetism, Institute of Physics,
University of Augsburg, D-86159 Augsburg, Germany*⁴*Department of Inorganic Polymers, “Petru Poni” Institute of Macromolecular Chemistry, Romanian Academy, 700487 Iasi, Romania*⁵*Felix Bloch Institute for Solid-State Physics, Leipzig University, 04103 Leipzig, Germany* (Received 2 June 2022; revised 28 August 2022; accepted 7 November 2022; published 18 November 2022)

We report crystal structure, magnetization, and specific heat measurements on single crystals of the hexagonal polar magnet $\text{Co}_{2-x}\text{Zn}_x\text{Mo}_3\text{O}_8$ magnetically diluted by replacing Co by Zn. In contrast to the transformation from the antiferromagnetic to a ferrimagnetic state observed in the isostructural $\text{Fe}_2\text{Mo}_3\text{O}_8$ upon small Zn doping, a robust antiferromagnetic behavior is preserved in Zn-doped $\text{Co}_2\text{Mo}_3\text{O}_8$ up to $x = 0.55$. The Néel temperature decreases from $T_N = 40$ K at $x = 0$ to 23 K at $x = 0.55$, thus extrapolating to $x = 1.27$ (36% filling) as the percolation threshold typical for a three-dimensional, highly coordinated network. This indicates strong magnetic couplings beyond the honeycomb planes in $\text{Co}_2\text{Mo}_3\text{O}_8$. A sharp peak in the specific heat and a clear cusp in the susceptibility associated with the onset of magnetic order is observed up to $x = 0.55$, whereas at $x = 0.66$ these features are broadened due to increased disorder. Interestingly, the in-plane lattice parameter, the Curie-Weiss temperature, and the magnetic entropy vary with x in a concerted but nonmonotonic manner. These observations can be traced back to the observed site-selective Zn substitution. We found that in the low-doping regime ($x < 0.2$) Zn^{2+} ions primarily occupy the octahedrally coordinated sites, although they have a clear preference for occupying the tetrahedrally coordinated sites at higher doping levels. Due to the multiple interlayer exchange paths, dependent on the coordination of the Co^{2+} ions, this behavior is reflected in the nonmonotonic variation of the Curie-Weiss temperature and magnetic entropy with substitution.

DOI: [10.1103/PhysRevB.106.174421](https://doi.org/10.1103/PhysRevB.106.174421)**I. INTRODUCTION**

Ternary molybdenum oxides containing $3d$ transition metals with the general formula $\text{Me}_2\text{Mo}_3\text{O}_8$ ($\text{Me} = \text{Mn}, \text{Fe}, \text{Co}$, and Ni) have recently attracted increasing interest due to a number of remarkable effects, such as hidden ferromagnetism [1], giant thermal Hall effect [2], strong linear and nonlinear magnetoelectric effects [3,4], giant magnetoelectricity in a state with collinear spin configuration [1,5], giant optical diode effect [6], optical magnetoelectric effect [7], coexistence of antiferromagnetism and ferrimagnetism in adjacent honeycomb layers [8], complex antiferromagnetic order [9], and orbital effects [10]. These materials crystallize in a hexagonal noncentrosymmetric crystal structure of the polar space group $P6_3mc$. Me^{2+} ions occupy two different cationic sites with tetrahedral and octahedral oxygen coordination. In the ab plane, the alternating tetrahedral and octahedral Me^{2+} ions form a honeycomb sublattice [Fig. 1(a)]. Along the c axis, the Me^{2+} ions also alternate and form linear chains [Fig. 1(b)]. A long-range antiferromagnetic (AFM) order is reported for all $\text{Me}_2\text{Mo}_3\text{O}_8$ compounds. The AFM ordering is ascribed solely to the $3d$ ions, while Mo ions form diamagnetic Mo_3O_{13} clusters [11]. The Néel temperature T_N is 60 K for $\text{Fe}_2\text{Mo}_3\text{O}_8$, 42 K for $\text{Mn}_2\text{Mo}_3\text{O}_8$, 40 K for $\text{Co}_2\text{Mo}_3\text{O}_8$ [12], and 6 K for $\text{Ni}_2\text{Mo}_3\text{O}_8$ [9].

Spin arrangement in the ground state of $\text{Me}_2\text{Mo}_3\text{O}_8$ depends on the type of the $3d$ ion. Earlier neutron powder-diffraction measurements revealed similar magnetic structures in $\text{Co}_2\text{Mo}_3\text{O}_8$ and $\text{Fe}_2\text{Mo}_3\text{O}_8$, with the spins of the tetrahedral and octahedral ions arranged antiferromagnetically in the honeycomb layers in the ab plane and ferromagnetically in the chains spanning along the c axis [12,13]. In $\text{Mn}_2\text{Mo}_3\text{O}_8$, a ferrimagnetic spin configuration with an antiparallel spin alignment both in the ab plane and along the c axis was proposed. A more complex spin structure consisting of both stripy and zigzag AFM orders in the ab plane was recently revealed in $\text{Ni}_2\text{Mo}_3\text{O}_8$ [9]. Such a diversity of the ground-state spin configurations observed in compounds with the same crystal structure indicates complex exchange interactions and an exceptional tunability of this structure type. Indeed, Zn doping was successfully used to transform antiferromagnetic order in $\text{Fe}_2\text{Mo}_3\text{O}_8$ into ferrimagnetic [3,14], but little is known about relevant magnetic interactions in other $\text{Me}_2\text{Mo}_3\text{O}_8$ compounds and their evolution upon substitutions with nonmagnetic ions.

In the present paper, we report the isovalent substitution of magnetic Co^{2+} by nonmagnetic Zn^{2+} in $\text{Co}_{2-x}\text{Zn}_x\text{Mo}_3\text{O}_8$ single crystals grown for compositions up to $x = 0.66$. We observe a nonmonotonic variation of structural parameters as

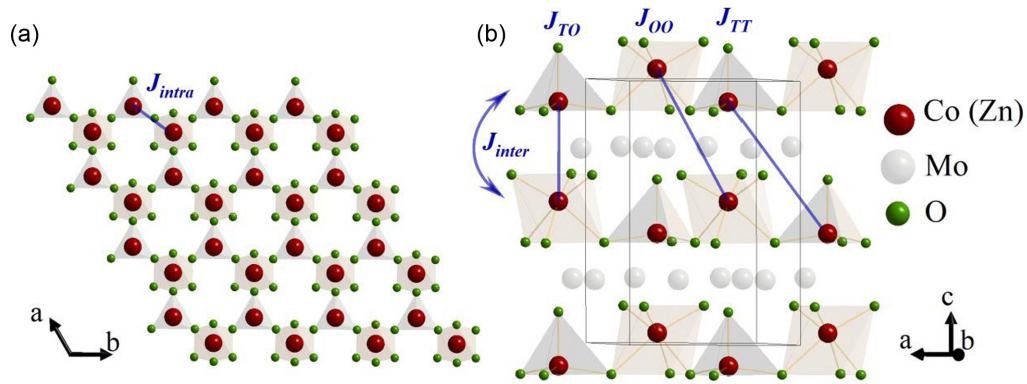


FIG. 1. Representation of the crystal structure of $\text{Co}_{2-x}\text{Zn}_x\text{Mo}_3\text{O}_8$: (a) in the ab plane and (b) in the ac plane. J_{intra} stands for the in-plane interaction between neighboring Co^{2+} ions at the octahedral and tetrahedral sites, while J_{OO} , J_{TT} , and J_{TO} are interplane interactions between Co^{2+} ions at two adjacent octahedral sites, at two neighboring tetrahedral sites, and at one octahedral and one tetrahedral site, respectively, which are considered in the present paper.

well as Curie-Weiss temperatures, whereas Néel temperature decreases continuously and extrapolates to zero at $x = 1.27$ as the percolation threshold. These trends are notably different from $\text{Fe}_{2-x}\text{Zn}_x\text{Mo}_3\text{O}_8$ where magnetic ground state changes upon Zn doping already at $x = 0.25$ [3,14]. We ascribe these effects to the site-selective Zn substitution. The Zn^{2+} ions preferentially occupy the tetrahedral sites, but may also enter the octahedral sites in the studied doping range, i.e., before the Zn substitution is completed at the tetrahedral sites.

II. METHODS

$\text{Co}_{2-x}\text{Zn}_x\text{Mo}_3\text{O}_8$ polycrystals were synthesized by solid-state reactions from high purity binary oxides CoO (99.999%), ZnO , and MoO_2 (99%) in evacuated quartz ampoules by repeated sintering at 1000°C . Single crystals were grown by the chemical transport reaction method at temperatures between 950 and 900°C using anhydrous TeCl_4 as a source of the transport agent. The growth was done in double quartz ampoules to prevent oxidation upon breaking the inner ampoule, which sometimes occurred close to the final stage of the growth. Single crystals up to 7 mm in size for pure $\text{Co}_2\text{Mo}_3\text{O}_8$ and up to 4 mm for Zn-substituted $\text{Co}_{2-x}\text{Zn}_x\text{Mo}_3\text{O}_8$ have been obtained after four weeks of transport.

Phase purity of the samples was checked by collecting x-ray powder diffraction data from polycrystals and crushed single crystals on an Empyrean diffractometer from PANalytical ($\text{Cu } K_\alpha$ radiation) using the Bragg-Brentano HD optics on the incident beam and the reduced energy window for the PIXCEL detector in order to suppress x-ray fluorescence of Co. The FULLPROF Suite program [15] was used for the refinement of the diffraction patterns.

High-resolution XRD data [16] were collected at the ID22 beamline of the European Synchrotron Radiation Facility (ESRF, Grenoble) using the wavelength of 0.35423 \AA and the multianalyzer detector setup. Powders obtained by finely grinding single crystals were loaded into thin-wall borosilicate glass capillaries and spun during the measurement. The JANA2006 program [17] was used for the structural refinement.

The single-crystal x-ray diffraction measurements were carried out with a Rigaku Oxford-Diffraction Xcalibur E CCD diffractometer equipped with graphite-monochromated $\text{Mo } K_\alpha$ radiation. The data were corrected for the Lorentz and polarization effects and for the absorption by multiscan empirical absorption correction methods. All structures, except the sample with $x = 0.55$, were refined by the full matrix least-squares method based on F^2 with anisotropic displacement parameters; the structure of the sample with $x = 0.55$ was refined in an isotropic approximation. The unit cell determination and data integration were carried out using the CRYSLIS package of Oxford Diffraction [18]. All calculations were carried out by the programs SHELXL2014 [19] and the WINGX software [20].

The chemical composition of the single-crystalline samples was analyzed by the ZEISS Crossbeam 550 using an energy dispersive x-ray spectroscopy (EDX) technique. The accuracy of the determination was about $\pm 5\%$.

The magnetic susceptibility and magnetization were measured by a superconducting quantum interference device magnetometer (MPMS 5, Quantum Design) between 2 and 400 K and magnetic fields up to 5 T. The specific-heat measurements were performed with the help of a physical properties measurement system (PPMS, Quantum Design) between 2 and 300 K in magnetic fields up to 9 T.

Density-functional band-structure calculations were performed in VASP [21–23] using the Perdew-Burke-Ernzerhof flavor of the exchange-correlation potential [24]. Correlation effects in the Co $3d$ shell were considered on the mean-field level via DFT + U with the on-site Coulomb repulsion parameter $U_d = 5$ eV, Hund's exchange $J_d = 1$ eV, and double-counting correction in the atomic limit [25–27].

III. RESULTS

A. Compositional analysis

The EDX analysis revealed that the actual concentration of Zn in the single crystals was significantly deviating from that in the starting polycrystalline material. The composition of the polycrystalline samples $\text{Co}_{2-x}\text{Zn}_x\text{Mo}_3\text{O}_8$ used for the growth of the single crystals is given in Table 1SM in the

TABLE I. Lattice parameters a and c for polycrystalline $\text{Co}_{2-x}\text{Zn}_x\text{Mo}_3\text{O}_8$ with the different substitution level x . R_{Br} , R_{f} , and χ^2 characterize the quality of the fit.

x (charge)	a , Å	c , Å	c/a	R_{Br} (%)	R_{f} (%)	χ^2
0	5.7677(2)	9.9112(2)	1.7184	5.76	4.84	2.11
0.1	5.7681(1)	9.9105(2)	1.71816	9.27	8.33	2.19
0.2	5.7687(1)	9.9103(2)	1.71794	7.00	5.58	2.59
0.4	5.7684(1)	9.9077(2)	1.71758	5.98	4.51	2.57
0.6	5.7687(1)	9.9064(2)	1.71727	4.75	3.87	2.46
0.8	5.7685(1)	9.9054(2)	1.71715	5.72	4.78	4.34
1.5	5.7712(1)	9.9097(2)	1.71709	4.73	4.04	3.39

Supplemental Material [28] together with the concentration of Zn in the single-crystalline samples as determined by the EDX analysis. Moreover, we noticed the irreproducibility in the substitution process: for single-crystalline samples from different batches grown from the same starting polycrystals in similar thermal conditions, different Zn concentrations were found. Such effects seem to be not exceptional for $\text{Co}_{2-x}\text{Zn}_x\text{Mo}_3\text{O}_8$ and occur in $\text{Fe}_{2-x}\text{Zn}_x\text{Mo}_3\text{O}_8$ [14] as well. This irreproducibility is probably related to a disproportionation of the quaternary oxide in the presence of the transport agent at high temperatures. Indeed, a substantial amount of the single-crystalline monoclinic MoO_2 and metallic Zn was found in the final product.

B. Crystal structure

First, we discuss the x-ray diffraction results obtained for polycrystalline samples to uncover the general trend in the change of the lattice parameters with substitution in $\text{Co}_{2-x}\text{Zn}_x\text{Mo}_3\text{O}_8$ using samples with well-established stoichiometry, which is easy to control in polycrystals. The x-ray diffraction patterns for these samples were characteristic for the single-phase material with small traces of nonreacted oxides (typically of the order of 1% and below; see Fig. 1SM in the Supplemental Material [28]). The refinement of the crystal structure was done within the hexagonal symmetry, space group $P6_3mc$. The structural parameters obtained from the refinement are summarized in Table I. The lattice parameter a reveals a slight initial increase with the substitution up to $x = 0.2$ and then it becomes nearly constant with further increasing x up to 0.8 (see also Fig. 2SM of the Supplemental Material [28]). At the same time, the lattice parameter c exhibits a monotonic decrease with x for this range of substitutions. For the substitution range $0 \leq x \leq 0.8$, the ratio c/a shows a continuous decrease. On the other hand, in the sample with $x = 1.5$ both lattice parameters exhibit a significant increase compared to the values obtained at $0 \leq x \leq 0.8$. Trying to uncover the distribution of dopant atoms, we varied the occupancy of Co and Zn on the tetrahedral and octahedral sites. However, no clear conclusion concerning the preferable site occupation could be obtained because of the weak contrast between Co and Zn and the limited accuracy of lab powder-diffraction data.

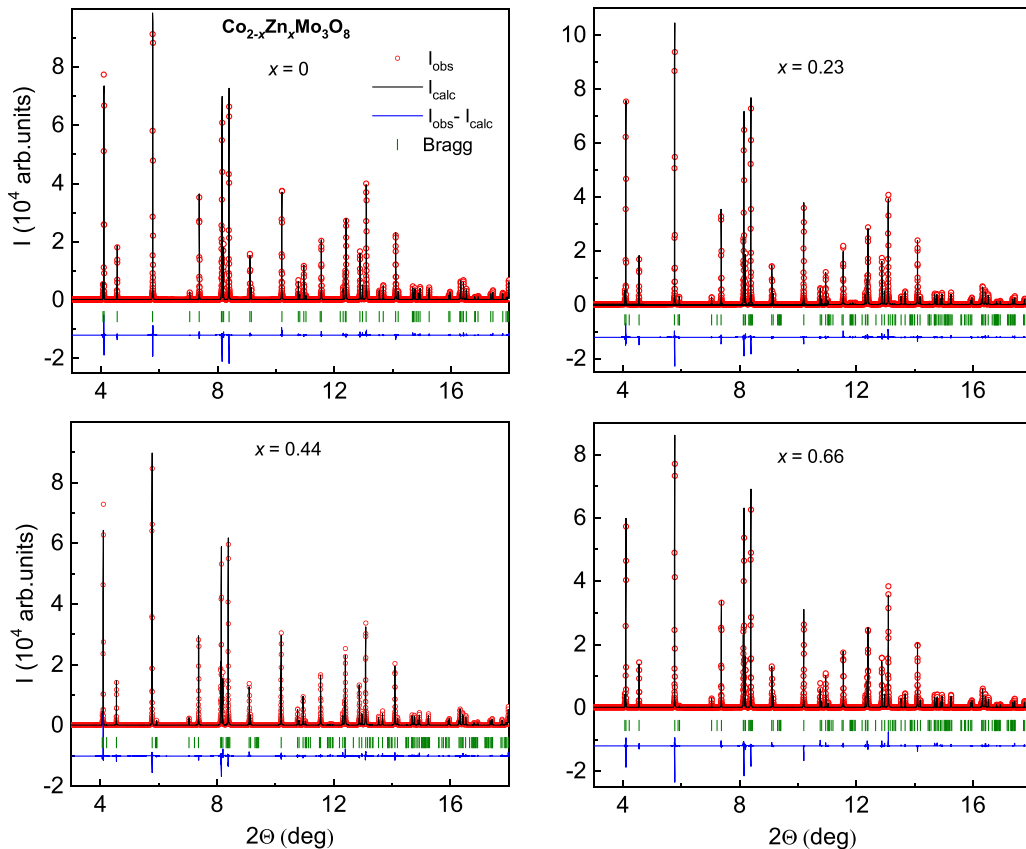


FIG. 2. High-resolution x-ray synchrotron powder diffraction patterns for the crushed single-crystalline $\text{Co}_{2-x}\text{Zn}_x\text{Mo}_3\text{O}_8$ samples with the different level of substitution.

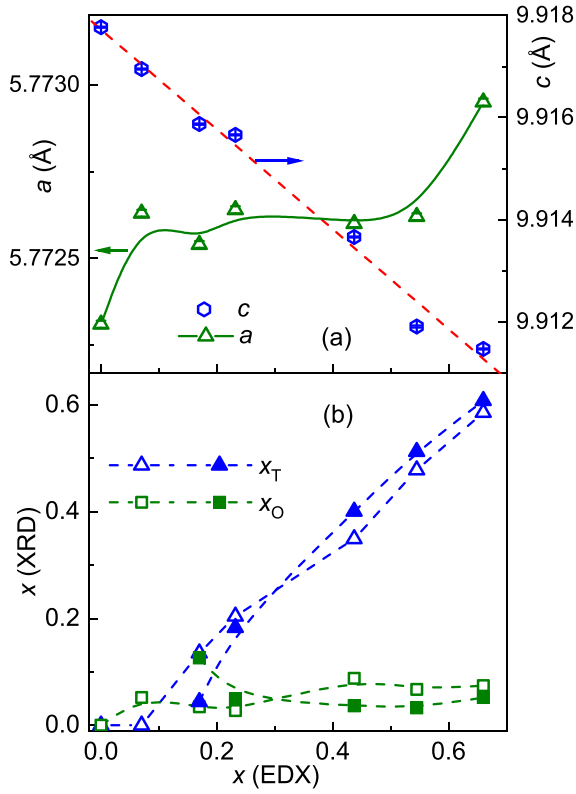


FIG. 3. (a) Lattice parameters a and c vs substitution level x in $\text{Co}_{2-x}\text{Zn}_x\text{Mo}_3\text{O}_8$ as obtained from the refinement of the high-resolution powder XRD data for crushed single crystals. The dashed line shows the linear fit to the c data. The error bars are less than the symbols size. (b) Concentrations of Zn^{2+} ions on the tetrahedral sites (x_T) and on the octahedral sites (x_O) vs substitution x obtained from the refinement of the high-resolution synchrotron XRD data (open symbols) and single-crystal XRD data (closed symbols). The sum of x_T and x_O is constrained to the EDX values. The connecting lines are a guide to the eye.

To reveal the distribution of Zn ions, we took advantage of the more sensitive techniques, single-crystal diffraction as well as high-resolution synchrotron diffraction performed on the same single-crystalline samples crushed into powders.

High-resolution data for several compositions of $\text{Co}_{2-x}\text{Zn}_x\text{Mo}_3\text{O}_8$ are shown in Fig. 2. Sharp reflections observed in all of the samples confirm the excellent homogeneity of our single crystals and the absence of any symmetry lowering with respect to the hexagonal space group $P6_3mc$. The lattice parameters a and c obtained from the structure refinement reveal the same trends as in the polycrystalline samples. With increasing the substitution level, the a parameter first shows a slight increase for $x = 0.07$ followed by a nearly constant value up to $x = 0.55$ and then increases again for $x = 0.66$ [Fig. 3(a)]. Although the overall change is minute, it is clearly discernible due to very high accuracy of the high-resolution synchrotron powder diffraction. A much larger change is observed for the c parameter that decreases monotonically up to at least $x = 0.66$ and extrapolates to $c = 9.8992$ Å at $x = 2$ (for complete substitution of Co by Zn). This value is clearly different from $c = 9.9219$ Å in the pure $\text{Zn}_2\text{Mo}_3\text{O}_8$ as measured under the

TABLE II. Lattice parameters a and c for single-crystalline $\text{Co}_{2-x}\text{Zn}_x\text{Mo}_3\text{O}_8$ with the different substitution level x as obtained from the refinement of the high-resolution synchrotron diffraction patterns. The error bars are from the Rietveld refinement

x (EDX)	a , Å	c , Å	c/a	R_{obs} (%)	R_p (%)	Goodness of Fit (GOF)
0	5.77231(1)	9.91777(1)	1.71816	2.34	5.87	2.32
0.07	5.77263(1)	9.91695(1)	1.71792	3.98	7.37	2.74
0.17	5.77254(1)	9.91587(1)	1.71776	2.98	6.87	2.44
0.23	5.77264(1)	9.91566(1)	1.7177	2.02	6.05	2.42
0.44	5.77260(1)	9.91366(1)	1.71736	2.41	6.32	2.36
0.55	5.77262(1)	9.91191(2)	1.71705	3.45	8.16	2.81
0.66	5.77295(1)	9.91147(1)	1.71688	3.04	6.59	2.33
2	5.77644(1)	9.92192(1)	1.71765	2.45	7.15	2.43

same experimental configuration. Therefore, we expect that above $x = 0.66$ the evolution of the c parameter becomes nonmonotonic, in agreement with the results for the $x = 1.5$ in polycrystalline sample (see Table II).

For a further analysis of the structural changes upon Zn doping, we performed a full structure refinement, where Zn atoms were initially placed in both octahedral and tetrahedral sites, with the total amount of Zn constrained to the value obtained from EDX. The resulting site occupancies, shown in Fig. 3(b) as a function of x , suggest the preferential doping into the tetrahedral site, although the sample with the lowest substitution level ($x = 0.07$) showed the opposite behavior, namely, the substitution into the octahedral site.

This trend in selective substitution was verified by single-crystal XRD. The experimental details and quality of refinement are presented in Table III. The Zn occupancies of the tetrahedrally and octahedrally coordinated sites, as obtained from the refinement of the single crystal x-ray diffraction data, are given in Table IV. The total amount of Zn ions on both cation sites was constrained to the value obtained from EDX. The resulting distribution of Zn between these two different sites is shown in Fig. 3(b). It is remarkably similar to the results obtained from the high-resolution synchrotron powder XRD data. At higher substitution levels, Zn atoms preferentially occupy the tetrahedral site, while below $x = 0.2$ the amount of Zn in the octahedral site exceeds that in the tetrahedral site.

This nontrivial evolution of the Zn occupancy on the tetrahedral and octahedral sites correlates with the evolution of the lattice parameter a that increases upon the initial substitution, remains constant above $x = 0.2$, and increases again above $x = 0.66$. Note that the ionic radius of the tetrahedrally coordinated Zn^{2+} (0.74 Å) is nearly equal to that of tetrahedral Co^{2+} (0.72 Å), contrary to the radius of the octahedrally coordinated Zn^{2+} (0.88 Å), which is much larger than that of the octahedral Co^{2+} (0.79 Å) [29,30]. Therefore, the substitution of Zn for Co at the octahedral sites is anticipated to result in a larger change of the lattice parameters compared to the substitution at the tetrahedral sites. Indeed, the constant value of the lattice parameter a below $x = 0.66$ suggests the preferential substitution into the tetrahedral site, as it indeed occurs above $x = 0.2$, but not at the lower substitution levels. This aspect will be further discussed in Sec. II E.

TABLE III. Summary of the crystallographic data and refinement details for the single-crystal XRD data collected on the samples of $\text{Co}_{2-x}\text{Zn}_x\text{Mo}_3\text{O}_8$.

	0.17	0.23	0.44	0.55	0.66
x (EDX)					
x-ray composition	$\text{Co}_{1.69}\text{Mo}_3\text{O}_8\text{Zn}_{0.31}$	$\text{Co}_{1.67}\text{Mo}_3\text{O}_8\text{Zn}_{0.33}$	$\text{Co}_{1.40}\text{Mo}_3\text{O}_8\text{Zn}_{0.60}$	$\text{Co}_{1.35}\text{Mo}_3\text{O}_8\text{Zn}_{0.67}$	$\text{Co}_{1.25}\text{Mo}_3\text{O}_8\text{Zn}_{0.76}$
Formula weight	535.68	536.10	537.54	537.99	538.51
a (Å)	5.760(1)	5.762(1)	5.779(1)	5.782(1)	5.764(1)
c (Å)	9.897(1)	9.902(1)	9.929(1)	9.924(1)	9.899(1)
Volume (Å ³)	284.35(2)	284.68(3)	287.14(3)	287.27(2)	284.85(4)
Z/ρ_{calc} (g cm ⁻³)	2/6.256	2/6.254	2/6.217	2/6.220	2/6.278
μ (mm ⁻¹)	12.557	12.583	12.809	12.893	13.107
Crystal size (mm)	$0.12 \times 0.10 \times 0.08$	$0.13 \times 0.13 \times 0.10$	$0.14 \times 0.11 \times 0.10$	$0.13 \times 0.10 \times 0.10$	$0.1 \times 0.08 \times 0.08$
θ range for data collection (°)	4.085–29.032	4.084–25.014	4.072–29.154	4.072–27.250	4.082–29.205
Reflections collected/unique	3528/314	3154/224	4378/326	4271/287	2159/308
	$R_{\text{int}} = 0.0309$	$R_{\text{int}} = 0.0496$	$R_{\text{int}} = 0.0440$	$R_{\text{int}} = 0.0650$	$R_{\text{int}} = 0.025$
Data/parameters	314/33	224/34	326/34	287/21	308/34
GOF	1.020	1.048	1.005	1.003	1.014
$R_1, wR_2[I > 2\sigma(I)]$	0.0303, 0.0745	0.0149, 0.0372	0.0243, 0.0584	0.0269, 0.0628	0.0116, 0.0260
wR_2 (all data)	0.0745	0.0372	0.0584	0.0628	0.0260

C. Magnetic susceptibility and magnetization

Figure 4 presents the temperature dependence of the magnetic susceptibility χ , measured in a magnetic field of 1 T on the single-crystalline samples. The susceptibility is shown for two orientations of the applied magnetic field, perpendicular ($H \perp c$) and parallel ($H \parallel c$) to the c axis. For all samples a significant anisotropy of the χ_{\perp} and χ_{\parallel} was observed already in the paramagnetic state. The inset of Fig. 4(a) shows these data for the sample with $x = 0$. Despite this large anisotropy, the nonlinearity of the inverse susceptibility for both field orientations in the temperature range 100–300 K was found to be small. Thus, we used the Curie-Weiss (CW) fits to the experimental data for calculation of the effective magnetic moment μ_{eff} and the Curie-Weiss temperature θ_{CW} . While more complex models may be eventually needed to capture details of Co^{2+} multiplets on each of the octahedral and tetrahedral sites and fit magnetic susceptibility over a broader temperature range, the Curie-Weiss fits allow an initial assessment of changes in the magnetism upon Zn doping.

For samples with $0 \leq x \leq 0.55$, the susceptibility χ_{\parallel} exhibits a well-defined maximum on approaching the transition into the AFM state at T_{N} . The value of T_{N} was found to decrease continuously from 39.7 K for $x = 0$ to 22.9 K for $x = 0.55$ [Fig. 5(a)]. A weak maximum in χ_{\parallel} was further detected at 17.2 K for $x = 0.66$. Moreover, for samples within

TABLE IV. Zn occupancy of tetrahedrally and octahedrally coordinated sites in $\text{Co}_{2-x}\text{Zn}_x\text{Mo}_3\text{O}_8$. The accuracy of the refinement is given in the brackets.

x (EDX)	Zn occupancy of octahedrally coordinated sites	Zn occupancy of tetrahedrally coordinated sites
0.17	0.23(10)	0.08(9)
0.23	0.07(9)	0.26(10)
0.44	0.05(12)	0.55(12)
0.55	0.04(13)	0.63(13)
0.66	0.06(6)	0.70(6)

the substitution range $0.17 \leq x \leq 0.55$, both χ_{\perp} and χ_{\parallel} show an additional upturn at temperatures below 10 K, which becomes more pronounced with increasing x . This upturn masks the maximum in the in-plane susceptibility χ_{\perp} at T_{N} , which is hardly discernible already for $x = 0.44$ and 0.55 , while the maximum in the out-of-plane susceptibility χ_{\parallel} at T_{N} is still clearly visible for these compositions. The low-temperature susceptibility upturn can be significantly suppressed by the field of 5 T, thus indicating paramagnetic impurities as the probable cause. However, anisotropic behavior of this quasiparamagneticlike susceptibility below 10 K for the substituted samples does not support this assumption. We speculate that the quasiparamagneticlike susceptibility may originate from the suppression of the AFM order in the honeycomb layers in the ab plane, while the order along the c axis is less affected.

The variations upon substitution of the Curie-Weiss temperature θ_{CW} calculated from the CW fits to the susceptibility data in the temperature range 150–300 K for the in-plane and out-of-plane directions of the applied field are shown in Fig. 5(b). The striking features of these dependencies are the very large difference in the values of θ_{CW} between the two orientations and its nonmonotonic change with substitution. The large difference in the values of θ_{CW} for the in-plane and out-of-plane orientations observed for our samples is consistent with the earlier data of McAlister and Strobel [11] for pure $\text{Co}_2\text{Mo}_3\text{O}_8$ and recent data on the same compound reported by Tang *et al.* [31]. Our values of θ_{CW} for the pure sample ($x = 0$) are close to those of the $\text{Co}_2\text{Mo}_3\text{O}_8$ sample of Tang *et al.* [31], although they fitted the susceptibility data by the CW law in a broader temperature range 50–300 K. Especially remarkable is the excellent match between our $\theta_{\text{CW}} = -125$ K and their $\theta_{\text{CW}} = -128.6$ K for the in-plane orientation, where the nonlinearity of the inverse susceptibility is significantly smaller than for the out-of-plane orientation (see Fig. 2 of Ref. [31]).

The Curie-Weiss temperature θ_{CW} together with the values of the calculated effective magnetic moment μ_{eff} for all measured single-crystalline samples are given in Table V. These parameters show a notable scattering for samples from the same batch, although their Néel temperatures were exactly the

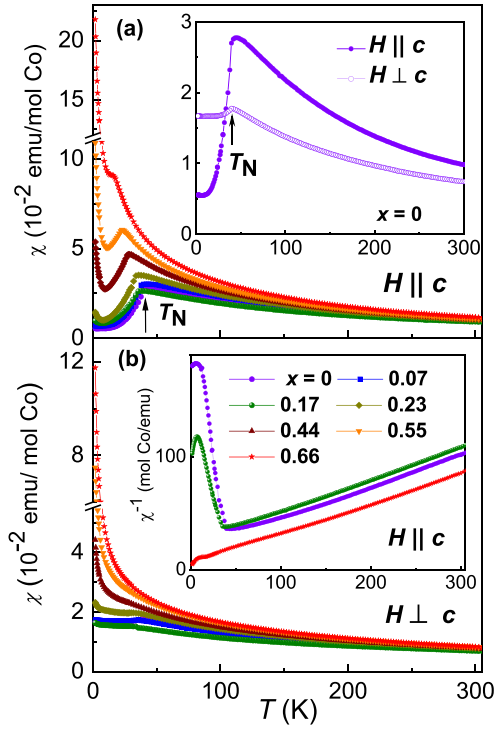


FIG. 4. Temperature-dependent magnetic susceptibility for $\text{Co}_{2-x}\text{Zn}_x\text{Mo}_3\text{O}_8$ samples measured in the field of 1 T, applied (a) parallel ($H \parallel c$) and (b) perpendicular ($H \perp c$) to the c axis. The inset in (a) shows the susceptibility vs temperature for both field orientations for the undoped sample ($x = 0$). The inset in (b) shows the inverse susceptibility vs temperature for $H \parallel c$ for samples with $x = 0, 0.17$, and 0.66 . The vertical arrow marks the Néel temperature T_N for sample with $x = 0$.

same. We attribute this scattering to a possible misalignment of the samples along the field direction due to the above-mentioned significant difference in the values of θ_{CW} for the in-plane and out-of-plane orientations that increases from a factor of 2.5 to 16 with an increase of the substitution level from $x = 0$ to $x = 0.66$. Taking the corresponding uncertainty into account as an error bar for the fitted values, we conclude that the effective moment does not change much, and Co^{2+} remains in the high-spin state with a significant orbital contribution to the magnetic moment: compare the experimental values of $5.3\text{--}5.6\mu_B$ with the spin-only value of $3.87\mu_B$ expected for spin $3/2$. Importantly, the effective moments are nearly the same for both field directions. The large anisotropy of the magnetic susceptibility is thus mainly caused by the very different Curie-Weiss temperatures measured for the in-plane and out-of-plane directions of the applied field. This difference reflects the strong single-ion anisotropy of Co^{2+} [32], which persists upon Zn^{2+} substitution.

A comparison of the nonmonotonic doping-level dependence of θ_{CW} reveals that the Curie-Weiss temperatures for both field orientations [Fig. 5(b)] reflect the behavior of the Co occupancy at the octahedral sites and mirror that of the Zn occupancy at these sites. At $x > 0.2$, the monotonic trend in θ_{CW} vs x is restored, and both θ_{CW} decrease in magnitude as the doping level increases. Their negative sign indicates predominant antiferromagnetic interactions up to $x = 0.55$.

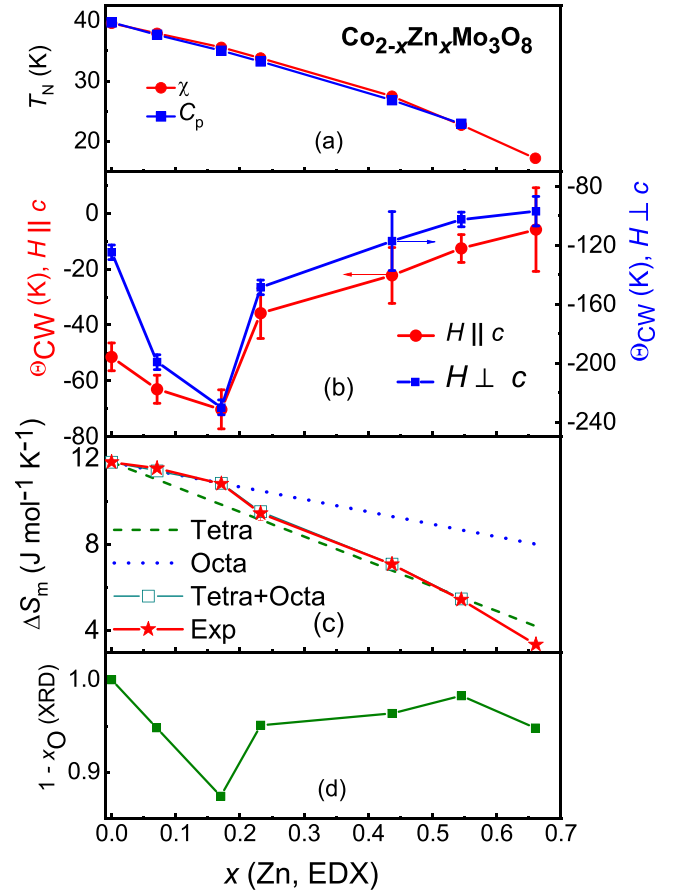


FIG. 5. Variation with the substitution level x : (a) of the Néel temperature T_N as extracted from the susceptibility and specific heat data, and (b) of the Curie-Weiss temperature θ_{CW} . Note the different scale for the left and right vertical axes in the plot for θ_{CW} vs x . (c) Variation of the magnetic entropy ΔS_m recovered at the AFM transition. The blue dotted line and the olive dashed line correspond to the dependence expected for the substitution of Zn for Co at the octahedral and tetrahedral sites, respectively (see text). (d) Site occupancy of Co ions on the octahedral sites, $(1 - x_O)$, vs substitution. x_O stands for the concentration of Zn at the octahedral sites.

Figures 6(a) and 6(b) show the magnetization curves at 2 K for the samples with the different level of substitution measured in static fields parallel and perpendicular to the c axis, respectively. The linear field dependence of M in the weakly doped samples ($x < 0.23$) is compatible with collinear antiferromagnetic order. Lower magnetization values for $H \parallel c$ for the low doping level suggest c as the easy-axis direction, similar to the parent compound $\text{Co}_2\text{Mo}_3\text{O}_8$. However, at higher doping levels the $M(H)$ curves become nonlinear, and magnetization values for $H \parallel c$ exceed those for $H \perp c$. This behavior parallels the quasiparamagnetic contribution to the susceptibility, as mentioned above.

D. Specific heat

Figures 7(a) and 7(b) show the temperature-dependent specific heat C_p measured in zero field on the single-crystalline samples with different substitution level at temperatures below 300 and 55 K, respectively. Also shown in these figures

TABLE V. Magnetic parameters (Néel temperature T_N , Curie-Weiss temperature θ_{CW} , effective magnetic moment μ_{eff} extracted from the Curie-Weiss fit to the magnetic susceptibility data *vs* temperature and averaged over several samples from the same batch. The accuracy of the calculation of θ_{CW} for a particular sample is below 1 K. The numbers in the brackets for the θ_{CW} and μ_{eff} reflect the scattering of these parameters for the samples from the same batch.

Substitution x (EDX)	T_N (K) ± 0.5 K	θ_{CW} (K) ($H \parallel c$)	μ_{eff} (μ_B/Co)		θ_{CW} (K) ($H \perp c$)	μ_{eff} (μ_B/Co) ($H \perp c$)
			($H \parallel c$)	($H \perp c$)		
0	39.7	-51 (± 5)	5.15		-125 (± 5)	5.09
0.07	37.7	-63 (± 5)	5.42		-199 (± 5)	5.53
0.17	35.0	-70 (± 7)	5.27		-230 (± 5)	5.66
0.23	33.2	-36 (± 9)	5.30		-149 (± 5)	5.32
0.44	26.8	-22 (± 10)	5.46		-117 (± 20)	5.39
0.55	22.9	-13 (± 5)	5.20		-103 (± 5)	5.14
0.66	17.2	-6 (± 15)	5.61		-97 (± 10)	5.59

is the specific heat measured on the single crystal of the diamagnetic isostructural compound $\text{Zn}_2\text{Mo}_3\text{O}_8$. From the comparison of these data, it is clear that above 55 K the specific heat for all $\text{Co}_{2-x}\text{Zn}_x\text{Mo}_3\text{O}_8$ samples is dominated by the phonon contribution.

Below 40 K, the specific heat for the samples with $0 \leq x \leq 0.55$ manifests a sharp λ -like anomaly at the magnetic transition at T_N . With increasing substitution, the λ -like anomaly at T_N is shifted to low temperatures in agreement with the shift of the susceptibility maximum [Figs. 4(a) and 5(a)]. The sample with the highest level of substitution, $x = 0.66$, exhibits only a broad anomaly centered at 17.4 K.

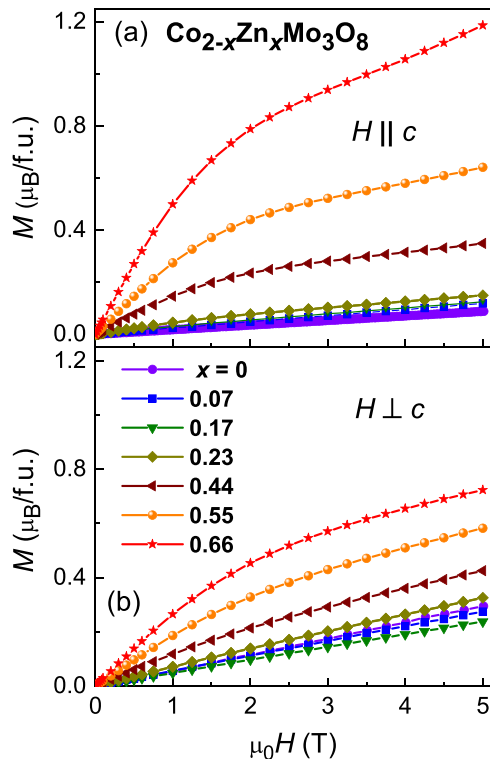


FIG. 6. Magnetization curves at 2 K for $\text{Co}_{2-x}\text{Zn}_x\text{Mo}_3\text{O}_8$ measured with the magnetic fields applied along (a) and perpendicular (b) to the c axis.

Figure 8 presents the effect of external magnetic field on the specific heat for the samples with the lowest and highest substitution. The field was applied along the c axis. Under magnetic fields, the λ -like anomaly in C for all samples with the substitution $x \leq 0.55$ exhibits a pronounced shift to lower temperatures as anticipated for the AFM state. In contrast, the sample with $x = 0.66$ shows only a hump that

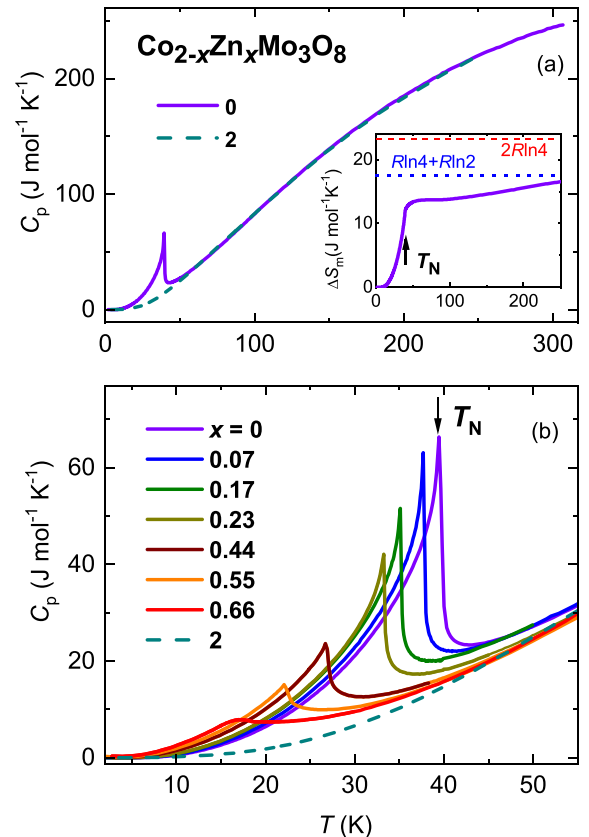


FIG. 7. Temperature dependence of the specific heat C_p for single-crystalline samples in zero magnetic field: (a) for $\text{Co}_2\text{Mo}_3\text{O}_8$ ($x = 0$, solid line) and diamagnetic $\text{Zn}_2\text{Mo}_3\text{O}_8$ ($x = 2$, dotted line) at temperatures below 300 K; (b) for samples $\text{Co}_{2-x}\text{Zn}_x\text{Mo}_3\text{O}_8$ with different x at temperatures below 55 K. Inset in (a) shows the temperature dependence of the magnetic entropy S_m for $\text{Co}_2\text{Mo}_3\text{O}_8$.

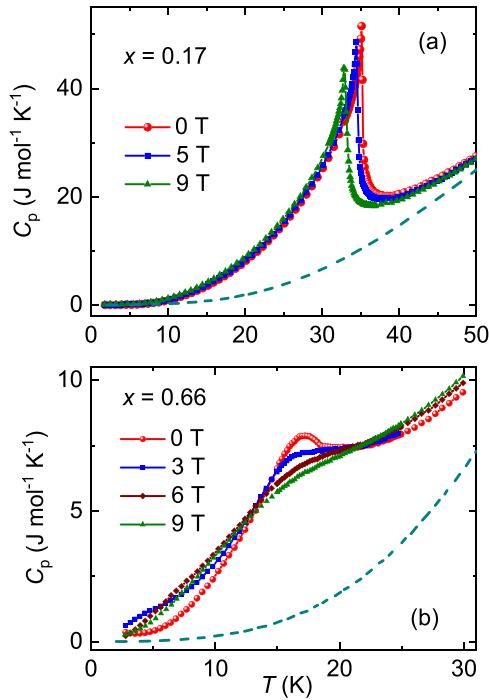


FIG. 8. Temperature dependence of the specific heat C for $\text{Co}_{2-x}\text{Zn}_x\text{Mo}_3\text{O}_8$ measured in different magnetic fields applied along the c axis: (a) $x = 0.07$; (b) $x = 0.66$. Dotted lines show the phonon contribution to specific heat.

is suppressed by increasing fields that no longer resembles the λ -like anomaly.

The magnetic entropy ΔS_m was calculated by integrating the magnetic part of the specific heat C_m/T vs T . The values of C_m were determined by subtracting the phonon contribution C_{lat} from the total specific heat and are shown in Fig. 4SM(a) of the Supplemental Material [28]. For C_{lat} we used the data for $\text{Zn}_2\text{Mo}_3\text{O}_8$ scaled by $\sim 1\%$ to correct for the difference in the molar masses of $\text{Zn}_2\text{Mo}_3\text{O}_8$ and $\text{Co}_{2-x}\text{Zn}_x\text{Mo}_3\text{O}_8$.

The temperature-dependent magnetic entropy for undoped $\text{Co}_2\text{Mo}_3\text{O}_8$ is shown in the inset of Fig. 7(a). Here, the magnetic entropy ΔS_m recovered at the AFM transition reached $11.8 \text{ J}/(\text{mol K})$. This value is $\sim 50\%$ less than the expected entropy of $2R \ln(2S + 1)$, or $2R \ln 4$, for two Co^{2+} ions with $S = 3/2$ per formula unit (model 1). The calculated entropy ΔS_m recovered at T_N is also only $\sim 67\%$ of $R \ln 4 + R \ln 2$ if the octahedral Co^{2+} ions at low temperatures are considered as an effective $J = 1/2$ system (model 2) following microscopic models established for several antiferromagnetic compounds containing Co^{2+} ions at the octahedral sites [33]. Above 65 K, the integral of C_m/T vs T becomes temperature independent and does not increase at least up to 90 K. However, the entropy in this range is still only $\sim 80\%$ of $R(\ln 2 + \ln 4)$ and $\sim 60\%$ of $2R \ln 4$. Moreover, above 90 K the entropy starts increasing again without any tendency to saturation: it increases by more than 10% up to 250 K. Assuming that the lattice contribution to the specific heat at high temperatures is evaluated correctly, this large gain of the entropy above 90 K indicates a significant magnetic contribution that may arise from the gradual occupation of the excited single-ion states and transformation of

the octahedrally coordinated Co^{2+} from $J = 1/2$ to $S = 3/2$ upon heating.

The temperature dependencies of the magnetic entropy for $\text{Co}_{2-x}\text{Zn}_x\text{Mo}_3\text{O}_8$ samples with different x are given in Fig. 4SM(b) in the Supplemental Material [28]. The evolution of the magnetic entropy ΔS_m recovered at T_N with substitution x is shown in Fig. 5(c). With increasing substitution, ΔS_m shows a nonlinear decrease in function of x . It cannot be explained by model 1, which assumes equal contributions to the entropy from both octahedral and tetrahedral sites. At the same time, it can be well fitted within model 2 under an assumption of the selective substitution of Zn for Co at different cationic sites. The dotted and dashed lines in Fig. 5(c) show the expected variation of the entropy ΔS_m upon substitutions on the octahedral and tetrahedral sites, respectively. At low substitution levels ($x \leq 0.17$), the experimental values of ΔS_m fall on the line corresponding to the octahedral sites. At higher x , the concomitant substitution on both cationic sites accounts for the variation of ΔS_m . For example, for the sample with $x = 0.23$, the experimental value of ΔS_m can be fitted with the Zn substitution $x = 0.065$ at the octahedral and substitution $x = 0.165$ at the tetrahedral sites. For the sample with $x = 0.44$, the change of the magnetic entropy can be fitted with the substitution $x = 0.05$ at the octahedral and $x = 0.39$ at the tetrahedral sites. For $x = 0.55$, Zn should substitute Co predominantly at the tetrahedral sites. The simulated data are shown by open squares in Fig. 5(c). The calculated concentrations of Zn ions redistributed between the octahedral and tetrahedral sites agree well with those obtained from the crystal structure analysis [Fig. 3(b)].

Although model 2 can account for the variation of the magnetic entropy with the substitution, the strongly reduced value of ΔS_m compared to the expected theoretical value needs further clarification. To get insight into this problem, we analyzed the behavior of the specific heat under applied magnetic fields. We found that at 50 K all $C_p(T)$ curves for different fields converge (not shown here). Together with the absence of any additional field-induced anomaly up to the fields of 9 T, this indicates the absence of any hidden ordering in the ground state. Moreover, at temperatures well above the transition region we obtained a perfect entropy balance for the specific heat data for $H = 0$ and $H = 9$ T, which can be an additional proof for the absence of the hidden order. These exclude the hidden order as a possible source of the missing magnetic entropy. It must be also noted that at temperatures above T_N the analysis of the specific heat must consider the contributions related to the crystal-field and spin-orbit coupling effects, which are important for the octahedral Co^{2+} ions. Another plausible reason is the short-range AFM order within the honeycomb layers that can persist to temperatures well above T_N , again leading to the incomplete recovery of the magnetic entropy at T_N . This deserves further study to uncover the origin of the missing entropy.

E. Energetics of Zn substitution

To assess changes in lattice energy upon Zn substitution, we constructed a twofold supercell and computed total energies for different distributions of the Zn^{2+} ions (Fig. 9), with the atomic positions in each configuration fully relaxed.

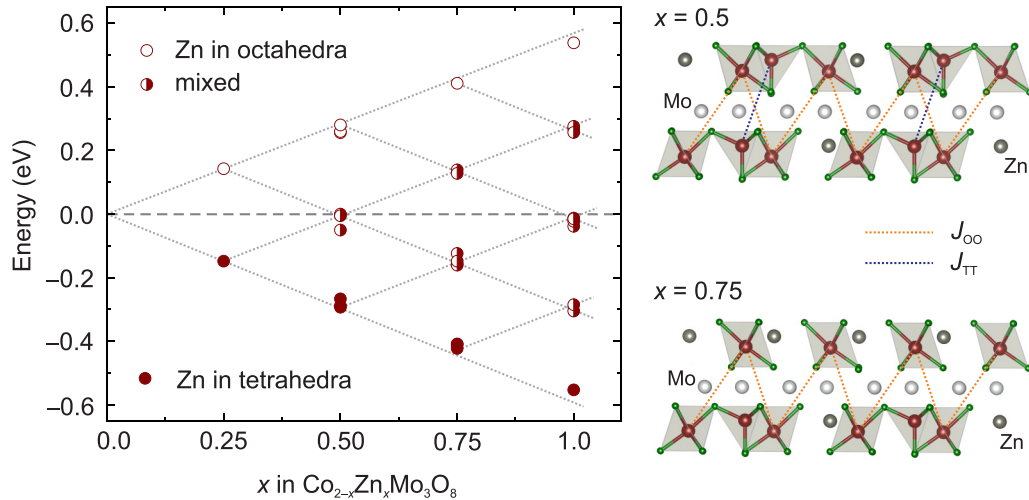


FIG. 9. Left: energies of the $\text{Co}_{2-x}\text{Zn}_x\text{Mo}_3\text{O}_8$ solid solution relative to the mixture of $\text{Co}_2\text{Mo}_3\text{O}_8$ and $\text{Zn}_2\text{Mo}_3\text{O}_8$ with the same composition. The dotted lines are extrapolations based on the constant energy of the Co/Zn substitution at the tetrahedral (-0.15 eV) or octahedral ($+0.15$ eV) sites. Right: representative local configurations show that the depletion of tetrahedral sites results in ferrimagnetic clusters (octahedron-tetrahedron-octahedron) or single octahedra and predominance of ferromagnetic couplings J_{OO} over antiferromagnetic J_{TT} . These clusters and single octahedra may be responsible for the quasiparamagnetic response observed at $x > 0.23$.

Doping one Zn atom ($x = 0.25$) results in an energy gain of about 0.15 eV/Zn for the tetrahedral site and about an equal energy loss for the octahedral sites. At higher doping levels, the energies follow the same trend and can be roughly estimated via a simple additive scheme (-0.15 eV and $+0.15$ eV for each Zn^{2+} ion doped in the tetrahedral and octahedral sites, respectively). However, starting from $x = 0.5$ some of the mixed configurations with both tetrahedral and octahedral sites occupied by Zn^{2+} also become energetically favorable (i.e., they are more stable than the mixture of $\text{Co}_2\text{Mo}_3\text{O}_8$ and $\text{Zn}_2\text{Mo}_3\text{O}_8$). An entropy term will additionally stabilize such mixed configurations, because configuration entropy increases when Zn is distributed between the octahedral and tetrahedral sites. Therefore, thermodynamic arguments predict the initial substitution into the tetrahedral sites followed by the gradual substitution into the octahedral sites at higher Zn concentrations.

The experimental situation is somewhat different. The XRD data and the nonmonotonic evolution of the magnetic parameters (Curie-Weiss temperature, magnetic entropy) both suggest Zn substitution into the octahedral sites below $x = 0.2$. Although such a configuration appears to be thermodynamically unfavorable, it is realized probably due to a combined initial increase in the parameter a and only a slight decrease of the lattice parameter c , allowing Zn to enter the octahedral sites. At higher substitution levels, above $x = 0.2$ and upon the stronger decrease of the c parameter, Zn atoms predominantly occupy the tetrahedral sites, as expected from thermodynamic arguments. Above $x = 0.5$, also the octahedral sites may be occupied, as suggested by the further increase in the lattice parameter a and by the gradual stabilization of the mixed configurations.

IV. DISCUSSION

Magnetic dilution of Co by Zn leads to a gradual suppression of the antiferromagnetic order in $\text{Co}_2\text{Mo}_3\text{O}_8$ with

the linear reduction in T_N . Extrapolation to $T_N = 0$ returns the percolation threshold at $x = 1.27$ that corresponds to the 36% filling of the magnetic sites. This value is much lower than the typical percolation thresholds in 2D lattices (for example, $x_c \sim 0.7$ in the honeycomb lattice) and compares well with the simple cubic lattice ($x_c \sim 0.3$) and other 3D lattices where each magnetic site has $-$ six to seven neighbors [34]. The low percolation threshold confirms the importance of interlayer exchange couplings in $\text{Co}_2\text{Mo}_3\text{O}_8$. Indeed, DFT calculations reveal the 3D coupling scenario with the in-plane coupling $J_{\text{intra}} = 18$ K and the interlayer couplings $J_{TT} = 10.7$ K, $J_{OO} = -1.7$ K, and $J_{OT} = -0.1$ K [8]. This interaction regime is not readily anticipated from the crystal structure because the metal-metal distance of nearly 6 Å for J_{TT} and J_{OO} is almost twice longer than 3.4 Å for J_{intra} .

We now elaborate on the scenario of the Zn^{2+} substitution. The replacement of the tetrahedrally coordinated Co^{2+} ions reduces the coupling energy by eliminating some of the strong bonds, J_{intra} and J_{TT} . The overall connectivity of the lattice is not affected, though, because the octahedral sites remain connected by J_{OO} . On the other hand, the ferromagnetic nature of J_{OO} suggests that a different type of magnetism may develop in regions where tetrahedral sites are strongly depleted, and weak ferromagnetic interactions become predominant. Representative local configurations shown in Fig. 9 suggest that at $x = 0.5$ ferrimagnetic stripes with two octahedra per one tetrahedron will form instead of the honeycomb layers. At $x = 0.75$, one also expects single octahedra that are coupled by ferromagnetic J_{OO} only. This scenario may explain the quasiparamagnetic low-temperature response observed at $x > 0.23$. It is also worth noting that the Curie-Weiss temperatures, θ_{CW} for $H \parallel c$, would cross zero much earlier than the percolation threshold is reached [Fig. 5(b)]. This also indicates the gradual crossover toward weak ferromagnetic couplings J_{OO} upon Zn substitution. A further replacement of the tetrahedrally coordinated Co^{2+} ions by Zn^{2+} should ultimately lead to a cation-ordered and ferromagnetic $\text{CoZnMo}_3\text{O}_8$ dominated by

J_{OO} , similar to the ferromagnetic $\text{FeZnMo}_3\text{O}_8$ reported previously [14]. However, this limit is never reached because a fraction of Zn^{2+} ions enters the octahedral sites and leads to disordered magnetism already at $x = 0.66$.

Finally, we comment on the spin state of the Co^{2+} ions in $\text{Co}_2\text{Mo}_3\text{O}_8$. Our high-field magnetization measurements reveal the saturation magnetization of $3\mu_B/\text{Co}$ [8] that suggests the $S = 3/2$ (high-spin) state for both tetrahedral and octahedral Co^{2+} ions. DFT calculations further evidence a strong single-ion anisotropy on the octahedral site [8] and imply a sizable splitting between the two Kramers doublets, such that at low temperatures and in low magnetic fields only the lower doublet ($J = 1/2$ state) becomes relevant. On the other hand, the tetrahedral Co^{2+} ion shows only a small splitting (and, correspondingly, a weak single-ion anisotropy in DFT [8]) and behaves as $S = 3/2$. This is consistent with our analysis of the magnetic entropy upon doping. A qualitatively similar scenario with two very different single-ion anisotropies on the tetrahedrally and octahedrally coordinated ions has been proposed for $\text{Ni}_2\text{Mo}_3\text{O}_8$ (see Fig. 9 in Ref. [9]).

V. CONCLUSION

In conclusion, our structural, magnetic, and specific heat studies of $\text{Co}_{2-x}\text{Zn}_x\text{Mo}_3\text{O}_8$ system with substitution of Zn^{2+}

for Co^{2+} in the honeycomb planes revealed a robust antiferromagnetically ordered ground state that extends over a wide range of substitutions, $x \leq 0.55$. This state manifests itself by a cusp in the susceptibility and a sharp peak in the specific heat. The Néel temperature shows a continuous decrease with increasing substitution. The AFM order gives way to a disordered magnetic state around $x = 0.66$. We found correlated nonmonotonic variations of the lattice parameter a , the asymptotic Curie-Weiss temperature, and the magnetic entropy with substitution, which are assumed to originate from the site-selective substitution of Zn for Co. The low percolation threshold of about 36% extrapolated from the doping dependence of T_N suggests 3D nature of the spin lattice with the strong interlayer couplings in $\text{Co}_2\text{Mo}_3\text{O}_8$.

ACKNOWLEDGMENTS

This work was supported by the Deutsche Forschungsgemeinschaft (DFG) through Transregional Research Collaboration TRR 80 (Augsburg, Munich, and Stuttgart) as well as by the project ANCD 20.80009.5007.19 (Moldova). We acknowledge ESRF for providing the beam time for this project and thank A. Fitch, C. Dejoie, and O. Grendal for their technical help during the measurement.

-
- [1] Y. Wang, G. L. Pascut, B. Gao, T. A. Tyson, K. Haule, V. Kiryukhin, and S.-W. Cheong, Unveiling hidden ferrimagnetism and giant magnetoelectricity in polar magnet $\text{Fe}_2\text{Mo}_3\text{O}_8$, *Sci. Rep.* **5**, 12268 (2015).
- [2] T. Ideue, T. Kurumaji, S. Ishiwata, and Y. Tokura, Giant thermal Hall effect in multiferroics, *Nat. Mater.* **16**, 797 (2017).
- [3] T. Kurumaji, S. Ishiwata, and Y. Tokura, Doping Tunable Ferrimagnetic Phase with Large Linear Magnetoelectric Effect in a Polar Magnet $\text{Fe}_2\text{Mo}_3\text{O}_8$, *Phys. Rev. X* **5**, 031034 (2015).
- [4] T. Kurumaji, S. Ishiwata, and Y. Tokura, Diagonal magnetoelectric susceptibility and effect of Fe doping in the polar ferrimagnet $\text{Mn}_2\text{Mo}_3\text{O}_8$, *Phys. Rev. B* **95**, 045142 (2017).
- [5] Y. S. Tang, S. M. Wang, L. Lin, C. Li, S. H. Zheng, C. F. Li, J. H. Zhang, Z. B. Yan, X. P. Jiang, and J.-M. Liu, Collinear magnetic structure and multiferroicity in the polar magnet $\text{Co}_2\text{Mo}_3\text{O}_8$, *Phys. Rev. B* **100**, 134112 (2019).
- [6] S. Yu, B. Gao, J. W. Kim, S.-W. Cheong, M. K. L. Man, J. Madéo, K. M. Dani, and D. Talbayev, High-Temperature Terahertz Optical Diode Effect without Magnetic Order in Polar $\text{FeZnMo}_3\text{O}_8$, *Phys. Rev. Lett.* **120**, 037601 (2018).
- [7] S. Reschke, D. G. Farkas, A. Strinić, S. Ghara, K. Guratinder, O. Zaharko, L. Prodan, V. Tsurkan, D. Szaller, S. Bordács, J. Deisenhofer, and I. Kézsmárki, Confirming the trilinear form of the optical magnetoelectric effect in the polar honeycomb antiferromagnet $\text{Co}_2\text{Mo}_3\text{O}_8$, *npj Quantum Mater.* **7**, 1 (2022).
- [8] D. Szaller, L. Prodan, K. Geirhos, V. Felea, Y. Skourski, D. Gorbunov, T. Förster, T. Helm, T. Nomura, A. Miyata, S. Zherlitsyn, J. Wosnitza, A. A. Tsirlin, V. Tsurkan, and I. Kézsmárki, Coexistence of antiferromagnetism and ferrimagnetism in adjacent honeycomb layers, [arXiv:2202.04700](https://arxiv.org/abs/2202.04700).
- [9] J. R. Morey, A. Scheie, J. P. Sheckelton, C. M. Brown, and T. M. McQueen, $\text{Ni}_2\text{Mo}_3\text{O}_8$: Complex antiferromagnetic order on a honeycomb lattice, *Phys. Rev. Mater.* **3**, 014410 (2019).
- [10] S. Reschke, A. A. Tsirlin, N. Khan, L. Prodan, V. Tsurkan, I. Kézsmárki, and J. Deisenhofer, Structure, phonons, and orbital degrees of freedom in $\text{Fe}_2\text{Mo}_3\text{O}_8$, *Phys. Rev. B* **102**, 094307 (2020).
- [11] S. P. McAlister and P. Strobel, Magnetic order in $\text{M}_2\text{Mo}_3\text{O}_8$ single crystals ($M = \text{Mn, Fe, Co, Ni}$), *J. Magn. Magn. Mater.* **30**, 340 (1983).
- [12] H. Czeskleba, P. Imbert, and F. Varret, Mössbauer Study of $\text{Fe}_2\text{Mo}_3\text{O}_8$ and $\text{FeZnMo}_3\text{O}_8$, in *Magnetism and Magnetic Materials — 1971 Parts 1 and 2*, AIP Conf. Proc. No. 5, edited by C. D. Graham and J. J. Rhyne (AIP, Woodbury, NY, 1972), pp. 811–815.
- [13] D. Bertrand and H. Kerner-Czeskleba, Etude structurale et magnetique de molybdates d'elements de transition, *J. Phys. (Paris)* **36**, 379 (1975).
- [14] S. Nakayama, R. Nakamura, M. Akaki, D. Akahoshi, and H. Kuwahara, Ferromagnetic behavior of $(\text{Fe}_{1-y}\text{Zn}_y)_2\text{Mo}_3\text{O}_8$ ($0 \leq y \leq 1$) induced by nonmagnetic Zn substitution, *J. Phys. Soc. Jpn.* **80**, 104706 (2011).
- [15] J. Rodríguez-Carvajal, Recent advances in magnetic structure determination by neutron powder diffraction, *Phys. B (Amsterdam, Neth.)* **192**, 55 (1993).
- [16] A. A. Tsirlin, L. Prodan, V. Tsurkan, and A. Fitch, High-resolution x-ray diffraction measurements for the $(\text{Co, Zn})_2\text{Mo}_3\text{O}_8$ solid solutions, European Synchrotron Radiation Facility (ESRF), doi: [10.1515/ESRF-DC-764180263](https://doi.org/10.1515/ESRF-DC-764180263).

- [17] V. Petříček, M. Dušek, and L. Palatinus, Crystallographic Computing System JANA2006: General features, *Z. Kristallogr.* **229**, 345 (2014).
- [18] CrysAlisPro Software System, Version 1.171.41.118a (Rigaku, Oxford, UK, 2015).
- [19] G. M. Sheldrick, Crystal structure refinement with SHELXL, *Acta Crystallogr. Sect. C* **71**, 3 (2015).
- [20] L. J. Farrugia, *WinGX* suite for small-molecule single-crystal crystallography, *J. Appl. Crystallogr.* **32**, 837 (1999).
- [21] K. Koepnik and H. Eschrig, Full-potential nonorthogonal local-orbital minimum-basis band-structure code, *Phys. Rev. B* **59**, 1743 (1999).
- [22] G. Kresse and J. Furthmüller, Efficiency of ab-initio total energy calculations for metals and semiconductors using a plane-wave basis set, *Comput. Mater. Sci.* **6**, 15 (1996).
- [23] G. Kresse and J. Furthmüller, Efficient iterative schemes for *ab initio* total-energy calculations using a plane-wave basis set, *Phys. Rev. B* **54**, 11169 (1996).
- [24] J. Perdew, K. Burke, and M. Ernzerhof, Generalized Gradient Approximation Made Simple, *Phys. Rev. Lett.* **77**, 3865 (1996).
- [25] H. Wu, M. W. Haverkort, Z. Hu, D. I. Khomskii, and L. H. Tjeng, Nature of Magnetism in $\text{Ca}_3\text{Co}_2\text{O}_6$, *Phys. Rev. Lett.* **95**, 186401 (2005).
- [26] M. Lenertz, J. Alaria, D. Stoeffler, S. Colis, A. Dinia, O. Mentré, G. André, F. Porcher, and E. Suard, Magnetic structure of ground and field-induced ordered states of low-dimensional $\alpha\text{-CoV}_2\text{O}_6$: Experiment and theory, *Phys. Rev. B* **86**, 214428 (2012).
- [27] H. J. Xiang, E. J. Kan, S.-H. Wei, M.-H. Whangbo, and X. G. Gong, Predicting the spin-lattice order of frustrated systems from first principles, *Phys. Rev. B* **84**, 224429 (2011).
- [28] See Supplemental Material at <http://link.aps.org/supplemental/10.1103/PhysRevB.106.174421> for details of preparation, composition characterization by EDX, results of structural studies by conventional x ray and single crystal x ray, and evaluation of the magnetic entropy.
- [29] R. D. Shanon and C. T. Prewit, Effective ionic radii in oxides and fluorides, *Acta Crystallogr. B* **25**, 925 (1969).
- [30] H. Abe, A. Sato, N. Tsujii, T. Furubayashi, and M. Shimoda, Structural refinement of $T_2\text{Mo}_3\text{O}_8$ ($T = \text{Mg, Co, Zn and Mn}$) and anomalous valence of trinuclear molybdenum clusters in $\text{Mn}_2\text{Mo}_3\text{O}_8$, *J. Solid State Chem.* **183**, 379 (2010).
- [31] Y. S. Tang, G. Z. Zhou, L. Lin, R. Chen, J. F. Wang, C. L. Lu, L. Huang, J. H. Zhang, Z. B. Yan, X. M. Lu, X. K. Huang, X. P. Jiang, and J.-M. Liu, Successive electric polarization transitions induced by high magnetic field in the single-crystal antiferromagnet $\text{Co}_2\text{Mo}_3\text{O}_8$, *Phys. Rev. B* **105**, 064108 (2022).
- [32] D. C. Johnston, Influence of uniaxial single-ion anisotropy on the magnetic and thermal properties of Heisenberg antiferromagnets within unified mean-field theory, *Phys. Rev. B* **95**, 094421 (2017).
- [33] J. C. Lashley, R. Stevens, M. K. Crawford, J. Boerio-Goates, B. F. Woodfield, Y. Qiu, J. W. Lynn, P. A. Goddard, and R. A. Fisher, Specific heat and magnetic susceptibility of the spinels GeNi_2O_4 and GeCo_2O_4 , *Phys. Rev. B* **78**, 104406 (2008).
- [34] S. C. van der Marck, Percolation thresholds and universal formulas, *Phys. Rev. E* **55**, 1514 (1997).